AGU PUBLICATIONS

JGR

Journal of Geophysical Research: Oceans

RESEARCH ARTICLE

10.1002/2016JC012590

Key Points:

- The equatorial jets in the Pacific Ocean decohere equatorward propagating semidiurnal internal tides
- The time-variable vertical shear flow and stratification cause incoherence on different time scales
- The equatorial jets do not cause increased internal tide dissipation in a 1/12.5° global ocean model

Supporting Information:

- Supporting Information S1
- Movie S1

Correspondence to:
M. C. Buijsman,
maarten.buijsman@usm.edu

Citation:
Buijsman, M. C., B. K. Arbic, J. G. Richman, J. F. Shriver, A. J. Wallcraft, and L. Zamudio (2017), Semidiurnal internal tide incoherence in the equatorial Pacific, *J. Geophys. Res. Oceans*, *122*, 5286–5305, doi:10.1002/2016JC012590.

Received 9 DEC 2016
Accepted 30 MAY 2017
Accepted article online 2 JUN 2017
Published online 3 JUL 2017

Semidiurnal internal tide incoherence in the equatorial Pacific

Maarten C. Buijsman[1], Brian K. Arbic[2], James G. Richman[3], Jay F. Shriver[4], Alan J. Wallcraft[4], and Luis Zamudio[3]

[1]Department of Marine Science, University of Southern Mississippi, Stennis Space Center, Mississippi, USA, [2]Department of Earth and Environmental Sciences, University of Michigan, Ann Arbor, Michigan, USA, [3]Center for Ocean-Atmospheric Prediction Studies, Florida State University, Tallahassee, Florida, USA, [4]Oceanography Division, U.S. Naval Research Laboratory, Stennis Space Center, Mississippi, USA

Abstract The jets in the equatorial Pacific Ocean of a realistically forced global circulation model with a horizontal resolution of 1/12.5° cause a strong loss of phase coherence in semidiurnal internal tides that propagate equatorward from the French Polynesian Islands and Hawaii. This loss of coherence is quantified with a baroclinic energy analysis, in which the semidiurnal-band terms are separated into coherent, incoherent, and cross terms. For time scales longer than a year, the coherent energy flux approaches zero values at the equator, while the total flux is ~500 W/m. The time variability of the incoherent energy flux is compared with the internal-tide travel-time variability, which is based on along-beam integrated phase speeds computed with the Taylor-Goldstein equation. The variability of monthly mean Taylor-Goldstein phase speeds agrees well with the phase speed variability inferred from steric sea surface height phases extracted with a plane-wave fit technique. On monthly time scales, the loss of phase coherence in the equatorward beams from the French Polynesian Islands is attributed to the time variability in the vertically sheared background flow associated with the jets and tropical instability waves. On an annual time scale, the effect of stratification variability is of equal or greater importance than the shear variability is to the loss of coherence. In the model simulations, low-frequency equatorial jets do not noticeably enhance the dissipation of the internal tide, but merely decohere and scatter it.

1. Introduction

Internal gravity waves generated by barotropic tidal motions over underwater topography, also referred to as internal tides, fill the world's oceans [*Dushaw et al.*, 1995; *Ray and Mitchum*, 1997; *Alford*, 2003; *Arbic et al.*, 2004; *Simmons et al.*, 2004a; *Shriver et al.*, 2012]. The internal tides that propagate long distances are mostly low mode waves [*Alford*, 2003], while the higher mode waves generally dissipate near their generation sites [*St. Laurent and Nash*, 2004]. The dissipation of internal tides contributes significantly to the diapycnal mixing of water masses [*Munk and Wunsch*, 1998]. However, quantifying precisely where the internal tides dissipate (at generation sites, in the open ocean, and/or at the continental shelves), and by what mechanisms they dissipate remains an open research question [*Ansong et al.*, 2015; *Buijsman et al.*, 2016; *MacKinnon et al.*, 2017]. Insight into these processes is relevant for developing mixing parameterizations for climate models because the three-dimensional geography and strength of mixing affects the overturning circulation in these models [*Simmons et al.*, 2004b; *Jayne*, 2009; *Melet et al.*, 2013].

Satellite altimetry of the ocean surface provides near-global coverage of low-mode internal tides [*Ray and Mitchum*, 1997; *Kantha and Tierney*, 1997; *Shriver et al.*, 2012; *Zhao et al.*, 2016; *Ray and Zaron*, 2016]. Satellite altimeter maps show internal tides propagating across basins for thousands of kilometers. However, the equatorial Pacific ocean appears to be a barrier of sorts for internal tides [*Carrére et al.*, 2004; *Shriver et al.*, 2012; *Zhao et al.*, 2016]. According to altimeter maps (Figure 1, replotted from *Shriver et al.* [2012]), neither beams that propagate southward from Hawaii or beams that propagate northward from the French Polynesian Islands (FPI), cross the equatorial Pacific. This may imply that the equatorial zonal jets cause a strong dissipation of the equatorward propagating internal tides. Another potential explanation for the equatorial demise of internal tides in altimetry maps is incoherence. The internal tide sea surface height signals are generally extracted from altimetry with a harmonic least-squares analysis over periods of several years [*Ray and Mitchum*, 1997; *Carrére et al.*, 2004; *Shriver et al.*, 2012; *Zhao et al.*, 2016; *Ray and Zaron*, 2016], and only

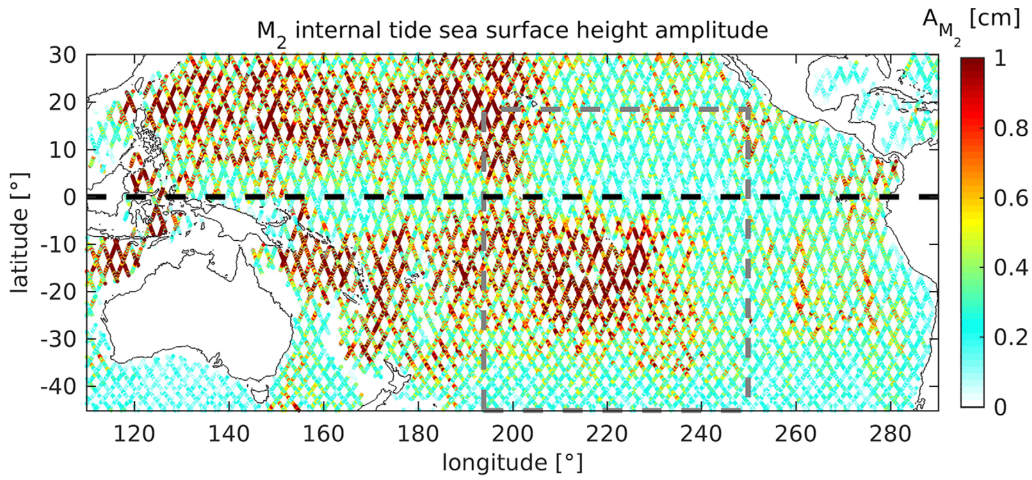

Figure 1. M_2 internal tide sea surface height amplitude extracted along 17 years of TOPEX/POSEIDON and Jason satellite altimetry tracks [see *Shriver et al*., 2012 for more details]. The equator is marked by the dashed black line. The area containing the French Polynesian Islands, for which we do monthly and annual analyses, is outlined by the gray dashed line.

the part of the total signal that is coherent with the barotropic narrow-band tidal forcing is retained. Using 23 years of satellite altimetry, *Zaron* [2017] determined that internal tides *do* exist in the equatorial Pacific and that more than 80% of the total semidiurnal internal tide signal is incoherent in this region. The existence of incoherent internal tides in the equatorial Pacific has also been demonstrated in global model simulations by *Savage et al*. [2017].

The equatorial jets in the Pacific are characterized by vertically and horizontally stacked zonal currents with alternating flow directions [*Firing et al*., 1998]. The dissipation rates at the equator are elevated in the upper water column [*Whalen et al*., 2012] and near the bottom [*Holmes et al*., 2016]. The causes of this dissipation are attributed to strong vertical shear of these zonal jets [*Peters et al*., 1988], surface heating and cooling cycles [*Smyth et al*., 2013; *Moum et al*., 2013], and near-bottom wave trapping and/or inertial instability [*Holmes et al*., 2016]. It has not yet been demonstrated that this dissipation can also be due to low-mode internal tides.

The decay of low-mode internal tides in the abyssal ocean may be caused by low to high mode scattering due to nonlinear wave-wave interactions [*Müller et al*., 1986; *MacKinnon et al*., 2013; *Müller et al*., 2015], topographic scattering [*Mathur et al*., 2014] (and references therein), and internal-tide mean-flow interactions [*Dunphy and Lamb*, 2014]. These scattered higher modes with smaller spatial scales are more susceptible to dissipation due to shear instabilities and overturning. The equatorward internal tides from the FPI propagate over relatively smooth topography [*Becker et al*., 2009]. Hence, topographic scattering most likely does not play a role near the equator, while wave-wave and wave-mean-flow interactions could be important for the demise of the internal tides. *Ivanov et al*. [1990] observed the scattering of semidiurnal internal tides to short period waves as the internal tide propagated across the equatorial jets in the Guiana basin. *Muench and Kunze* [2000] argue that momentum deposition from breaking small-scale internal waves could maintain the deep zonal jets.

Incoherent tidal motions have been observed in, e.g., coastal tide gauge records [*Munk and Cartwright*, 1966], velocity and density records from moorings [*Wunsch*, 1975; *van Haren*, 2004; *Zilberman et al*., 2011; *Nash et al*., 2012b; *Zaron and Egbert*, 2014; *Kelly et al*., 2015; *Stephenson et al*., 2015; *Ansong et al*., 2017], and satellite altimetry [*Ray and Zaron*, 2011; *Zaron*, 2015; *Zhao*, 2016; *Zaron*, 2017]. These incoherent motions have been attributed to internal tides that are not coherent with the tidal forcing. *Zaron* [2017] argues that up to 44% of the total semidiurnal internal tide signal in the world's oceans is incoherent. Because of their $\mathcal{O}(10$ day) sampling times, satellite altimeters do not easily allow for estimation of the incoherent tide amplitude at a particular location in the ocean. In contrast, eddy-resolving numerical models with realistic forcing allow for such local estimates [*Zaron and Egbert*, 2014; *Shriver et al*., 2014; *Kerry et al*., 2014, 2016; *Savage et al*., 2017]. Both *Zaron and Egbert* [2014] and *Shriver et al*. [2014] show that near the internal tide generation sites the internal tides are mostly coherent, and that they become more incoherent as they propagate away from the generation sites.

Several mechanisms contribute to the incoherence of internal tides. First, the internal tide generation (barotropic to baroclinic conversion) may vary in time with the tidal forcing due to local changes in stratification and/or remotely generated incoherent internal tides [*Chavanne et al*., 2014; *Nash et al*., 2012b; *Kelly et al*., 2015; *Pickering et al*., 2015; *Kerry et al*., 2014, 2016]. After generation, the internal tides propagate through mesoscale flows, and the associated spatial and temporal variability in stratification, currents, and vorticity may cause time variable refraction of the internal gravity wave fields [*Park and Watts*, 2006; *Rainville and Pinkel*, 2006; *Ward and Dewar*, 2010; *Zaron and Egbert*, 2014; *Dunphy and Lamb*, 2014; *Ponte and Klein*, 2015; *Kelly and Lermusiaux*, 2016; *Kelly et al*., 2016; *Kerry et al*., 2016; *Magalhaes et al*., 2016]. Hence, the internal tides become phase incoherent with the tidal forcing at a given location in the ocean. There are few studies that have looked into the interaction between the equatorial jets and the internal tides from the FPI and Hawaii. However, the interaction between midlatitude jets and internal tides has been studied in numerical model experiments [*Ponte and Klein*, 2015; *Kelly and Lermusiaux*, 2016; *Kelly et al*., 2016]. *Magalhaes et al*. [2016] attributed the seasonal variability of the internal tides from the Amazon shelf break, observed in satellite imagery, to the seasonal variability of the North Equatorial Counter Current.

From this discussion, we distill three questions that are addressed in this paper: (1) Can some of the internal-tide demise at the equator be attributed to the internal tides becoming incoherent after passing through the equatorial Pacific jets, and thus being missed by the least squares harmonic analysis? (2) What are the mechanisms of internal tide incoherence at the equator? (3) On what time scales do these mechanisms act? We address these questions using output from the latest global $1/12.5^\circ$ HYbrid Coordinate Ocean Model (HYCOM) simulations with realistic tidal and atmospheric forcing. Such models with realistic barotropic tides, internal tides, and mesoscale eddies may be used to examine the coherent and incoherent internal tide surface expression present in the wide swath altimetry obtained in future SWOT missions [*Fu and Ubelmann*, 2014]. We note that the $\sim$8 km horizontal resolution and 41 layers of HYCOM may not optimally resolve the dissipation associated with shear instabilities, wave breaking, and wave-wave and wave-mean flow interaction processes [*Müller et al*., 2015], which may occur at the equator. Hence, regarding question one, higher-resolution models may need to be applied to better address what fraction of the internal tide demise at the equator, seen in altimetry maps, is due to dissipation versus incoherence.

In the remainder of this paper, we first discuss the model and internal tide energy diagnostics. Next we diagnose the semidiurnal band-passed (total), the harmonically analyzed (coherent), and the residual (incoherent) energy fluxes radiating northward and southward from the FPI. We scrutinize the mechanisms that underlie internal-tide incoherence on monthly and annual time scales using the Taylor-Goldstein equation. We compare the Taylor-Goldstein-derived phase speeds with phase speeds computed with a plane-wave-fit method. In the last section, we present a discussion and conclusions.

2. Methodology

2.1. Numerical Model

We use a recent version of HYCOM (expt_06.1) to study the incoherence of the semidiurnal internal tide in the South Pacific. The simulation examined here employs atmospheric forcing from the Navy Global Environmental Model (NAVGEM) [*Hogan et al*., 2014] and geopotential tidal forcing for the three largest semidiurnal constituents (M_2, S_2, and N_2) and two largest diurnal constituents (K_1 and O_1). In theory, these five constituents can be separated with an hourly record that is 28 days or longer. The tidal forcing is augmented with a self-attraction and loading (SAL) term accounting for the load deformations of the solid earth and the self-gravitation of the tidally deformed ocean and solid earth [*Hendershott*, 1972; *Ray*, 1998]. The simulation features 41 layers in the vertical direction and a nominal horizontal resolution of $1/12.5^\circ$ at the equator. The simulation is started from an initial state on 1 July 2011. The initial state is obtained from running the model for 7 years with climatological forcing and then from 2003 to 2011 with the atmospheric forcing from the Navy Operational Global Atmospheric Prediction System (NOGAPS) [*Rosmond et al*., 2002]. Atmospheric NAVGEM forcing is applied after 30 June 2011. Tidal forcing is initiated on 3 July 2011. Global three-dimensional fields are stored every hour for a 1 year period from September 2011 to August 2012. We analyze a subset of this data set covering the Pacific Ocean between 45°S and 30°N. While the global data set requires about 150 tera bytes (TB) of storage, the subset amounts to 33 TB, including postprocessed data.

The simulation used here features several changes compared to our earlier HYCOM tidal simulations described in *Arbic et al*. [2010, 2012] and *Shriver et al*. [2012]. In this new simulation, an Augmented State Ensemble Kalman Filter (ASEnKF) technique is applied to reduce errors in the model's barotropic tidal sea surface elevations [*Ngodock et al*., 2016]. While the wave drag parameterization by *Garner* [2005] was used in our earlier simulations to account for unresolved high-mode internal wave generation and breaking, the parameterization by *Jayne and St. Laurent* [2001] is used in this simulation. Following *Buijsman et al*. [2015], this wave drag is tuned to minimize tidal sea surface elevation errors with respect to the TPXO8-atlas [*Egbert et al*., 1994]. We note that our results on coherence obtained with this new simulation with ASEnKF and the different drag scheme are qualitatively similar to those found in the prior simulations. In contrast with the older configuration of *Shriver et al*. [2012], the model bathymetry is extended to include the ocean under the floating Antarctic ice shelves. The changes described above have greatly lowered the area-averaged deep-water M_2 root-mean-square sea-surface error, from the 7.4 cm value in *Shriver et al*. [2012] to 2.6 cm in the simulation presented here.

2.2. Diagnostics

The generation, propagation, and dissipation of the semidiurnal internal tide is studied with the time-averaged and depth-integrated baroclinic energy equation [*Simmons et al*., 2004a; *Buijsman et al*., 2014]

$$\nabla \cdot \mathbf{F} + D = C, \tag{1}$$

where $\mathbf{F}=(F_x, F_y)$ are the fluxes in the x (east-west) and y (north-south) directions, D is dissipation, and C is the barotropic to baroclinic energy conversion. D is computed as the residual of the flux divergence and conversion terms. We can ignore the rate of change term as the period of averaging (month and year) makes this term orders of magnitude smaller than the terms in equation (1). Similarly, the internal-tide self-advection is also small [*Simmons et al*., 2004a; *Buijsman et al*., 2014]. However, we find dipoles of positive and negative flux divergence at the equatorial jets (not shown). *Kelly et al*. [2016] and *Kelly and Lermusiaux* [2016] show that these dipoles are balanced by energy terms related to energy advection by the mean flow. We do not compute these terms here; this work is saved for a future paper. In accordance with findings by *Ward and Dewar* [2010] and *Dunphy and Lamb* [2014], *Kelly and Lermusiaux* [2016] state that "energy advection by the mean flow does not produce a net volume-integrated energy transfer between the tide and mean flow, which explains the (nearly) offsetting regions of internal-tide energy sources and sinks". As we spatially average the energy terms, the energy loss and gain associated with the dipoles cancel and their impact is minimized. The time variability in the background flow causes a time variability in the dipoles and the energy fluxes. The time variability of these fluxes is the subject of this paper.

We follow the approach by *Nash et al*. [2012b] and *Pickering et al*. [2015] to compute the coherent and incoherent contributions to equation (1). For this purpose, we decompose the barotropic (depth-averaged) velocity according to

$$\mathbf{U}_{\mathrm{D2}} = \mathbf{U}_{\mathrm{coh}} + \mathbf{U}_{\mathrm{inc}}, \tag{2}$$

where $\mathbf{U}=(U, V)$ is the barotropic velocity with components U and V along the x and y directions, $_{\mathrm{D2}}$ refers to semidiurnal band-passing between 10 and 14 h, $_{\mathrm{coh}}$ is the coherent component obtained by harmonic least-squares fit of the M_2, S_2, and N_2 constituents to the band-passed time series, and $_{\mathrm{inc}}$ refers to the incoherent part. The incoherent term is computed as the difference between the band-passed and harmonic time series. Similarly the baroclinic velocities and perturbation pressures are, respectively, decomposed as

$$\mathbf{u}'_{\mathrm{D2}} = \mathbf{u}'_{\mathrm{coh}} + \mathbf{u}'_{\mathrm{inc}} \tag{3}$$

and

$$p'_{\mathrm{D2}} = p'_{\mathrm{coh}} + p'_{\mathrm{inc}}, \tag{4}$$

where the prime notation denotes a (baroclinic) departure from a (barotropic) depth-average. We then compute the time-mean and depth-integrated baroclinic energy flux and time-mean conversion terms as

$$\mathbf{F}_{D2} = \frac{1}{T}\int_T\int_H p'_{coh}\mathbf{u}'_{coh} + p'_{inc}\mathbf{u}'_{inc} + p'_{inc}\mathbf{u}'_{coh} + p'_{coh}\mathbf{u}'_{inc}\,dz\,dt \tag{5}$$

and

$$\begin{aligned} C_{D2} = \frac{1}{T}\int_T & -p'_{b,coh}\mathbf{U}_{coh}\cdot\nabla H \\ & -p'_{b,inc}\mathbf{U}_{inc}\cdot\nabla H \\ -p'_{b,inc}\mathbf{U}_{coh}\cdot\nabla H & - p'_{b,coh}\mathbf{U}_{inc}\cdot\nabla H\,dt, \end{aligned} \tag{6}$$

where p'_b is the perturbation pressure at the bottom, t is time, T is the period of integration, z is the vertical coordinate (positive upward), and H is the resting water depth. Each energy term comprises a coherent term, an incoherent term, and two cross terms. Although we differentiate between incoherent and cross-terms, the cross-terms have a negligible contribution after time averaging. The reader is referred to *Nash et al*. [2012b] for a discussion of the cross terms.

We use the percentage

$$\gamma = 100\frac{|\Theta_{D2} - \Theta_{coh}|}{|\Theta_{D2}|} \tag{7}$$

as a metric for the incoherence, where Θ is either energy flux or conversion. Maps of the metric given in equation (7) look similar to maps of the $R^2 - 1$ metric used by *Pickering et al*. [2015].

3. Model Results

3.1. Equatorial Pacific

The Pacific ocean with its tall underwater ridges, such as Hawaii, the Mariana Islands, Luzon Strait, and the FPI is an important generator of radiating low-mode internal tides [*Simmons et al*., 2004a; *Buijsman et al*., 2016]. The magnitudes of the semidiurnal band-passed fluxes averaged over 1 year, from September 2011 to August 2012, are displayed in Figure 2a. γ, the ratio of the sum of the incoherent and cross-term fluxes to the band-passed fluxes, is presented in Figure 2b. The equatorial Pacific stands out as a location of internal tide incoherence. As soon as the northward propagating internal tides from the FPI encounter the equator, they become incoherent. In contrast, the southward propagating waves from the FPI remain mostly coherent. The southward propagating internal tides from Hawaii and even the Mariana Islands also become incoherent after passing through the equatorial region. Some of the internal tides generated at the Mariana Islands and the Izu Ogasawara Ridge propagate more than 4000 km in an east-southeasterly direction. In contrast to the internal tides radiating equatorward from Hawaii and the FPI, the east-southeasterly propagating internal tides from the Mariana Islands and Izu Ogasawara Ridge maintain a high level of coherence over much larger distances. Another striking feature of Figure 2b is that as soon as one moves away from the main beams (even away from the equator, and even close to the generation sites), the incoherence increases from essentially zero to $\sim$20% values. This means that the internal tides are most coherent in the beams and right near the generation sites, and more incoherent elsewhere, in qualitative agreement with findings by *Zaron and Egbert* [2014] and *Shriver et al*. [2014].

In Figure 3, we present spectral properties for unfiltered time series of steric sea surface height along an internal tide beam radiating equatorward from the FPI. This beam is marked with ***a***-***b*** in Figure 2a. Steric sea surface height represents a depth-integral of the baroclinic motions, and it is often used to study internal tides [*Shriver et al*., 2012, 2014; *Ansong et al*., 2015; *Savage et al*., 2017]. The time series are split into three overlapping 6 month long segments and their power spectral densities are averaged to reduce noise levels. Within 7° from the generation site, south of $\sim$6°S, the steric sea surface height has little energy at subtidal motions (Figures 3a and 3c), while it features energetic narrow-band peaks at semidiurnal frequencies (Figures 3b and 3d). These tidal peaks are well-resolved by the least-squares harmonic fits (not shown). Equatorward of $\sim$6°S energetic mesoscale motions occur with periods larger than $\sim$5 days (Figure 3a). This coincides with the broadening of the tidal peaks and the shallowing of the tidal cusps (Figure 3b). The internal tide sea surface height amplitudes, in particular of M_2, quickly weaken near the equator (Figure 3b). To the north of the equator, the semidiurnal tidal peak has become very broad, masking the M_2, S_2 and N_2

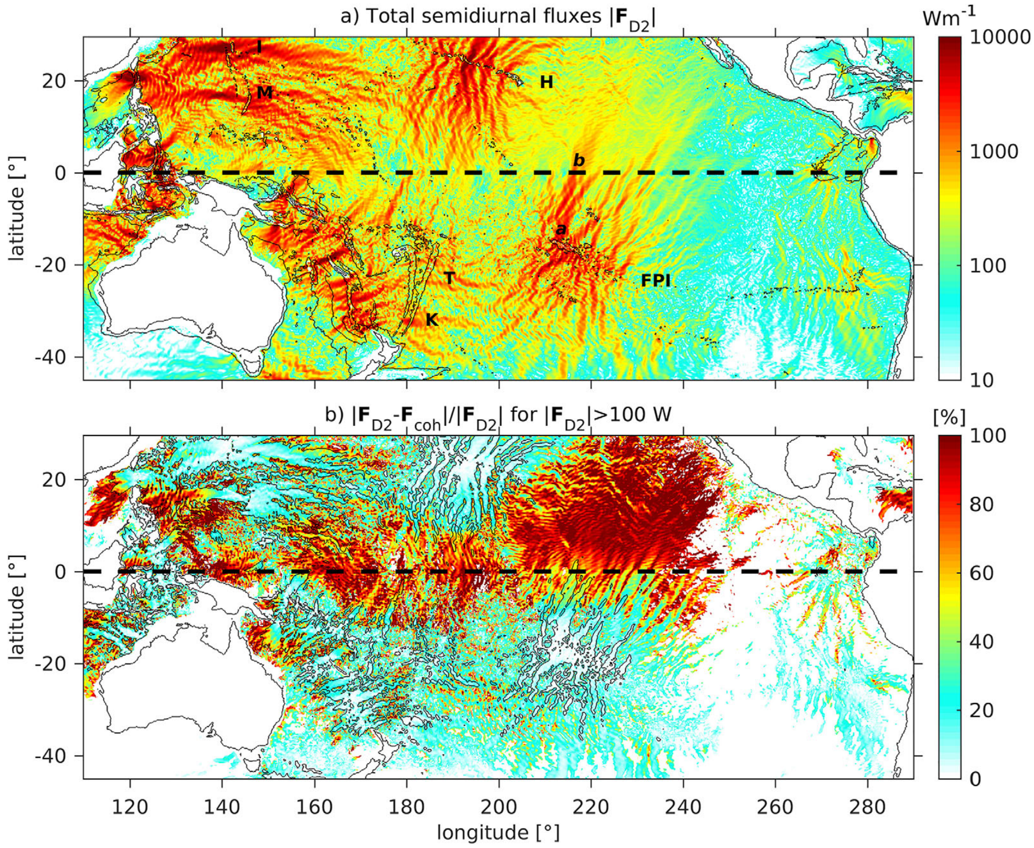

Figure 2. (a) The magnitude of the annual-mean semidiurnal band-passed energy fluxes in the equatorial Pacific from HYCOM. Bathymetry is contoured at 0 and −2000 m. Hawaii is abbreviated with **H**, the French Polynesian Islands with **FPI**, Tonga with **T**, the Kermadec Islands with **K**, the Izu Ogasawara Ridge with **I**, and the Mariana Islands with **M**. Spectral properties are computed along the internal tide beam marked by ***a*-*b***. (b) The percentage of the sum of the annual-mean incoherent and cross-term fluxes to the band-passed fluxes. Values coinciding with $|\mathbf{F}_{D2}| < 100$ W m^{-1} are not shown. The black contours mark 1000 W m^{-1} of the band-passed fluxes. Bathymetry is contoured at 0 m. In both subplots, the equator is marked by the dashed black line.

peaks (Figures 3b and 3d). The spectra in Figure 3 show a qualitative correlation between the presence of mesoscale motions and the broadening of the tidal peaks. The increase in internal-tide incoherence along the beam is associated with this broadening.

3.2. French Polynesia

In the remainder of this paper, we diagnose the internal tides radiating from the French Polynesian Islands (FPI; also called the Tuamotu Archipelago) in the South Pacific. We select this area for an in-depth analysis because of the strong contrast between the coherence of the northward and southward radiating internal tides from the FPI and because the internal tide generation and propagation are minimally affected by internal tides generated at other source regions. Figure 2a shows that the beams radiating from remote sources such as Hawaii and the ridges along the Tonga and Kermadec Trenches do not interfere with the internal tide generation sites at the FPI. However, we observe interference between eastward radiating energy flux beams from Hawaii with beams from the FPI north of the equator and between eastward flux beams from the Tonga and Kermadec Islands south of the FPI. The interference patterns in Figure 2 are characterized by alternating energy flux minima and maxima at horizontal scales smaller than a mode 1 wave length [*Martini et al*., 2007; *Buijsman et al*., 2014]. These spatial scales are much smaller than the spatial scale of the reduction in internal tide amplitude along the equator seen in the satellite altimetry in Figure 1. Moreover, a linear superposition of internal tide fluxes does not cause a loss of coherence. Therefore, wave interference should equally affect the magnitudes of both the band-passed and coherent fluxes. Since we observe differences between the band-passed and coherent fluxes in the equatorial region (Figure 2b), we

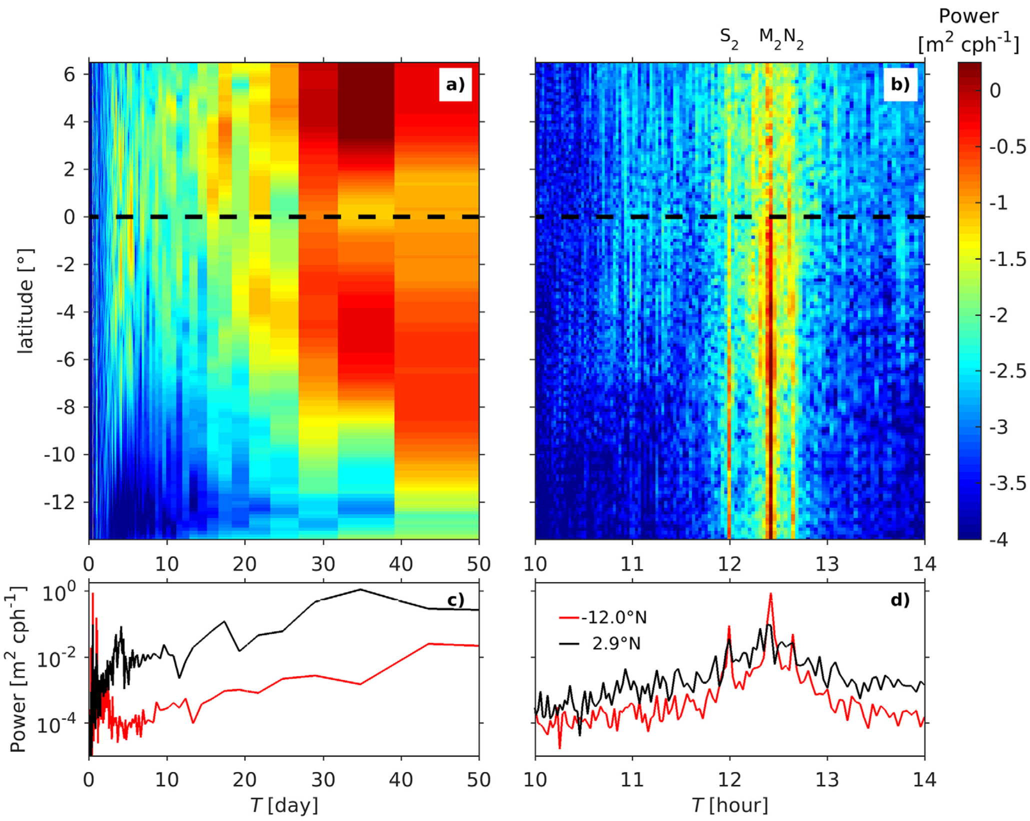

Figure 3. Power spectral density of steric sea surface height (a and b) along an internal tide beam and (c and d) for the nearfield (red) and far-field (black). The beam is marked with ***a-b*** in Figure 2a. Subplots (a) and (c) show the spectral properties for periods from 0 to 50 days and (b) and (d) show them for periods from 10 to 14 h. In (a) and (b), the dashed black lines mark the equator. The spectra are computed for three overlapping 6 month long windows using unfiltered time series.

argue that the reduced amplitudes in the satellite altimetry are due to a loss of coherence and not interference.

We compute time-mean energy flux and conversion terms every month and average them over 12 months (referred to as the "monthly mean") and for an entire year (referred to as the "annual mean"). The magnitudes of the annual-mean band-passed, coherent, incoherent, and cross-term fluxes are shown in Figures 4a–4d. While the band-passed fluxes extend northward across the equator, the coherent fluxes have decreased to virtually zero to the north of the equator (Figure 4b). This decrease of the coherent fluxes coincides with an increase in the incoherent fluxes (Figure 4c). In contrast to the results from monthly or shorter time-series, the cross-term fluxes computed for the annual time series are nearly zero (Figure 4d). Note that the minimum in the coherent energy fluxes (Figure 4b) and the maximum in the incoherence fraction γ (Figure 2b) occur in a zonal band north of the equator near 7°.

Next we spatially average the energy terms in bins along four transects: two transects to the north and two to the south of the FPI (Figure 4a). The along-transect length of the bins is about 275 km (about 2.5°) and the bin width varies from about 500 to 900 km, depending on the transect. To avoid crowding, we do not plot the individual bins in Figure 4a; only the outer bin boundaries are shown. Each transect is divided in nearfield and far-field boxes that are used in section 4. The bin-mean values are plotted along the western and eastern transects in Figures 5 and 6, respectively. In Figures 5a and 6a, the monthly mean band-passed fluxes (black solid curves) cannot be distinguished from the means computed for the annual time series (black dashed curves). The band-passed energy fluxes decrease in magnitude away from the FPI. A similar decrease is observed in altimetry-inferred fluxes [*Buijsman et al*., 2016]. The internal tide decay can be attributed to viscous, numeric, and wave-drag dissipation and radial spreading. In accordance with the results shown in Figure 4b, the monthly-mean coherent fluxes show a faster decline compared with the band-passed fluxes to the north of the FPI than they do to the south of the FPI along both the western and

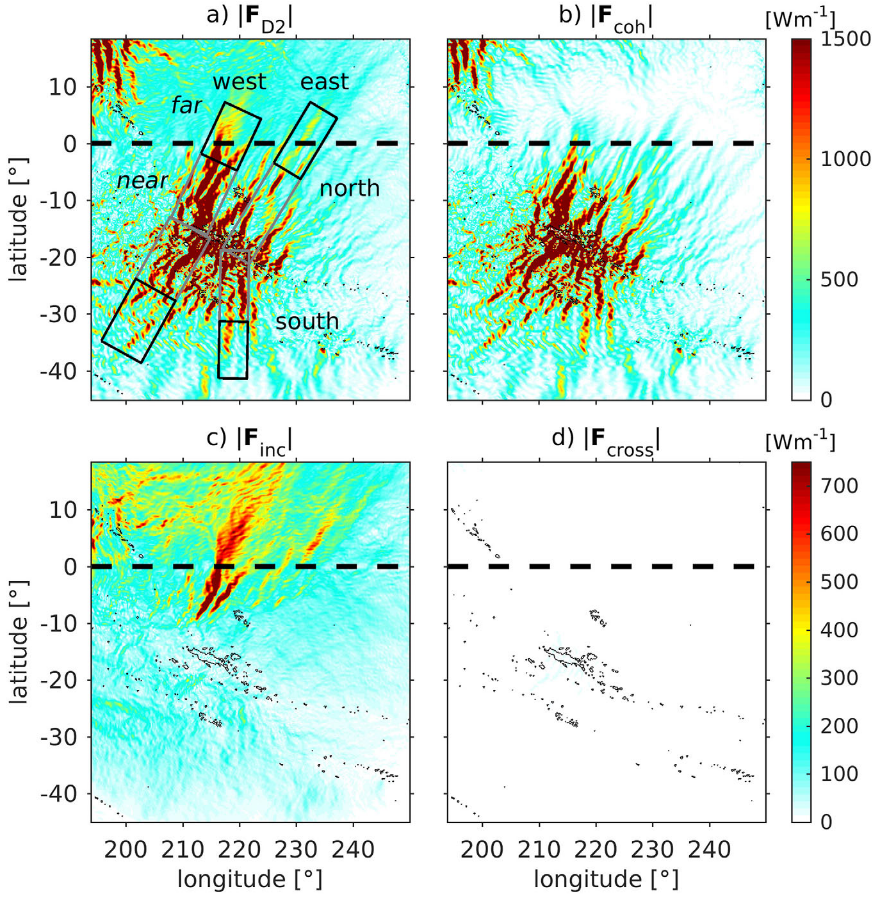

Figure 4. Semidiurnal baroclinic energy fluxes from the FPI averaged over 1 year (September 2011 to August 2012). The magnitude of the (a) band-passed, (b) coherent, (c) incoherent, and (d) cross-term fluxes. The boxes in Figure 4a mark the two transects to the north and the two transects to the south of the FPI. Each transect features a far and nearfield section, marked by black and gray lines, respectively. The black contours mark depths of 2000 m and the equator is marked by the dashed black line.

eastern transects. The annual-mean coherent fluxes (red dashed curves) decline faster in magnitude away from the source than the monthly mean coherent fluxes (red solid curves). The northward annual-mean coherent fluxes have become nearly zero at 5°N along both transects (see also Figure 4b). The inverse relation between coherent amplitude and record length has also been shown in *Colosi and Munk* [2006], *Nash et al.* [2012a], and *Ansong et al.* [2015]. *Ansong et al.* [2015] show that the coherent internal tide amplitude does not reach an equilibrium until record lengths approach about 3 years. This suggests that the coherent fluxes computed in this paper from 1 year of model output have not yet reached an equilibrium value, and are likely to further decrease for longer records.

As the difference between the band-passed and coherent fluxes increases away from the source, the incoherent terms increase in magnitude, in particular along the northward beams (blue curves in Figures 5b and 6b). The annual-mean incoherent fluxes are larger and increase closer to the source than the monthly mean fluxes. After the initial rapid increase in the incoherent fluxes, the fluxes plateau north of the equator. This may be because there is some contribution to the fluxes by more coherent internal tide beams, for example, from the Hawaiian Island ridge. The cross-term fluxes decline in amplitude away from the source in Figures 5b and 6b (magenta curves). In particular for the monthly mean fluxes, this decline is because the coherent pressure and velocity amplitudes, which are larger than the incoherent amplitudes, decline away from the generation sites. In contrast to the monthly-mean cross-term fluxes, the annual-mean cross-term fluxes are nearly zero. For longer time series, the coherent and incoherent terms of the cross-product become more uncorrelated, causing smaller mean values.

Similar to the energy flux, the annual-mean and monthly-mean internal tide dissipation computed from the band-passed fields decreases with distance from the FPI (not shown). The dissipation rates do not show an

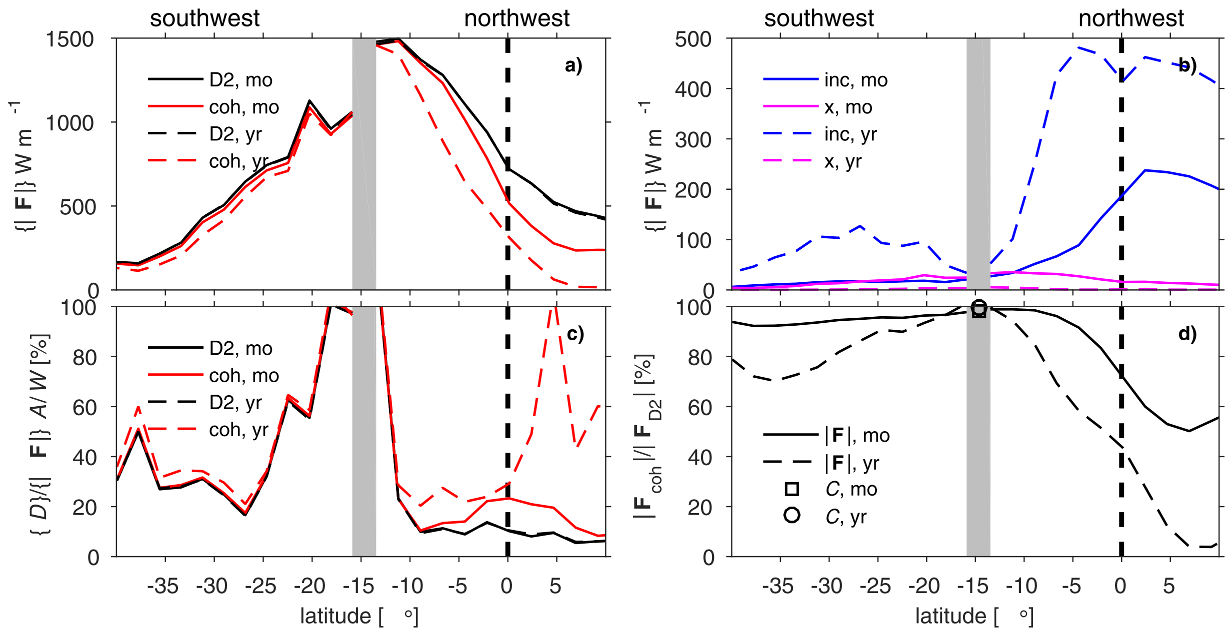

Figure 5. The magnitudes of the bin-averaged (a) band-passed and coherent and (b) incoherent and cross-term fluxes radiating away from the FPI, (c) fraction of the flux that dissipates, and (d) coherent fraction of the band-passed fluxes (curves) and conversion (symbols) for the western transects. The incoherent and cross terms are denoted by "inc" and "x" in Figure 5b. The flux is multiplied with bin width *W* and dissipation with bin area *A* in Figure 5c, so that their units are in Watts. The averaged monthly means are the solid curves and labeled with "mo." The means computed over the 1 year long-time series are the dashed curves and are labeled with "yr." The locations of the equator and FPI are marked by the black dashed lines and gray bars, respectively. In Figure 5a, the black-dashed curve is fully covered by the black solid curve.

increase near the equator, where the incoherent energy flux peaks (Figures 5b and 6b). As dissipation is proportional to wave energy and energy flux, we remove the effect of the declining energy flux by normalizing the bin-integrated dissipation by the bin-width integrated energy flux. This fraction along the western and eastern transects is plotted in Figures 5c and 6c. Values exceed more than 100% close to the FPI because we omit barotropic to baroclinic conversion in this fraction. The annual-mean and monthly mean fraction of the band-passed flux that dissipates (D2; black curves) is higher on the south than the north side of the FPI.

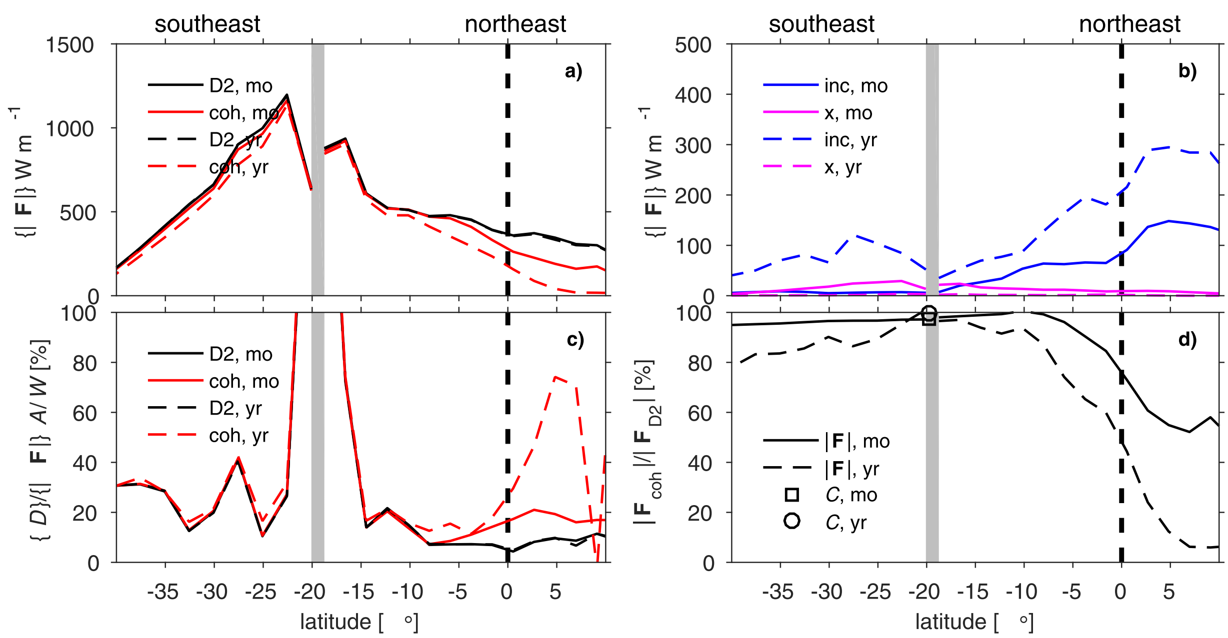

Figure 6. As in Figure 5, but for the eastern transects.

Similar to the dissipation, we do not observe an increase in the fraction of the semidiurnal energy flux that is dissipated at the equator. However, there is a significant increase in the dissipation of the coherent flux (red curves) at the equator between 0 and 5°, with the annual-mean peak being larger than the monthly-mean peak along both transects. This indicates that the coherent internal tide is being scattered into incoherent tides, in agreement with 5b and 6b. In contrast, south of the FPI no such abrupt increase is found and the differences between the coherent and band-passed fractional dissipation remain small.

The monthly and annual-mean fraction of the coherent flux (conversion) relative to the total flux (conversion) is shown in Figures 5d and 6d. On monthly and annual time scales, the barotropic to baroclinic conversion at the FPI is largely coherent (square and circle symbols), implying that the internal tides become incoherent as they propagate away from the FPI. Although the magnitude of the total and coherent fluxes in Figures 5d and 6d is larger along the western than the eastern transect, the magnitude of $|\mathbf{F}_{coh}|/|\mathbf{F}_{D2}|$ is nearly identical along both transects. The annual-mean $|\mathbf{F}_{coh}|/|\mathbf{F}_{D2}|$ drops off much closer to the FPI along the northwest transect as compared to the northeast transect, where $|\mathbf{F}_{coh}|/|\mathbf{F}_{D2}|$ remains relatively large between 20°S and 10°S. This difference can be attributed to the northwest-southeast orientation of the FPI and the mechanisms of incoherence that act in an area that is parallel to the equator. In accordance with prior discussion, the internal tides are more coherent to the south of the FPI, causing $|\mathbf{F}_{coh}|/|\mathbf{F}_{D2}| > 80\%$.

The supplemental material includes an animation showing the time evolution of semidiurnal band-passed fluxes that radiate equatorward and poleward from the FPI. In agreement with Figures 4–6, the poleward fluxes and the equatorward fluxes south of the equator remain largely coherent. South of the equator, the main horizontal flux beams (dark red colors) are fixed in place and demonstrate little temporal variability. However, the flux beams become strongly time variable north of the equator. Here, the beams oscillate laterally like "branches in the wind." Their lateral movements can be as much as a few degrees. In the months of September 2011 to January 2012, the flux beams from the FPI become more diffuse or "washed out" north of the equator (e.g., at 218°E and 0°N in Figure 2a). In contrast, in the subsequent months of February 2012 to August 2012, the flux beams are more coherent and radiate as far north as 15°N.

4. Mechanisms of Incoherence

4.1. Currents and Stratification

In the HYCOM simulations with realistic atmospheric forcing and astronomical tidal forcing, there is a striking loss of coherence in the propagating semidiurnal internal tides as they pass through the equatorial Pacific Ocean. The internal tides that propagate equatorward from the FPI quickly become incoherent with the astronomical tidal forcing, while the poleward beams remain largely coherent. We attribute the loss of coherence of the equatorward beams to the time variability of the equatorial jets. Over 1 year, from September 2011 through August 2012, we compute two-daily mean velocities, layer thicknesses, and densities. The annual-mean zonal velocity and its standard deviation for water depths up to 2 km along the western transects are presented in Figure 7. Along this transect, the equatorial jets are the most prominent features, and they display large and highly variable velocities and strong vertical shear. The north-south extent of the jets is about 1700 km (5°S—10°N). South of the FPI, as marked by the gray bar in Figure 7, the zonal flows and their variability are much smaller. Note that the jets' location is offset to the north of the equator, consistent with the greater amount of incoherence seen in the northern hemisphere noted earlier (see, for instance, Figure 2b).

Over the same year-long period, we compute 2 day mean kinetic energy $KE = \frac{1}{H}\int\int \bar{u}^2 + \bar{v}^2 dz dt$ and 2 day mean buoyancy frequency N averaged over the surface layer with a thickness of $H = 500$ m for the western and eastern transects, where $\bar{u}$ and $\bar{v}$ are the 2 day mean velocities. The time variability of KE and N is shown in Figure 8. In agreement with Figure 7b, the KE magnitude and variability are strongest in the equatorial jets. In the first 120 days of the simulation (September to January), the northwest transect displays 30–40 day oscillations of jet energy (Figure 8a), more so than at the northeast transect (Figure 8b). The power spectral density in Figure 3 also shows a peak near 35 days. These oscillations are associated with westward propagating tropical instability waves [*Philander et al.*, 1986]. These waves can also be associated with the relatively weak short-term variability of N at the equator (Figures 8c and 8d). However, the strongest variability in the surface-mean stratification is due to the seasonal cycle in solar radiation, which is

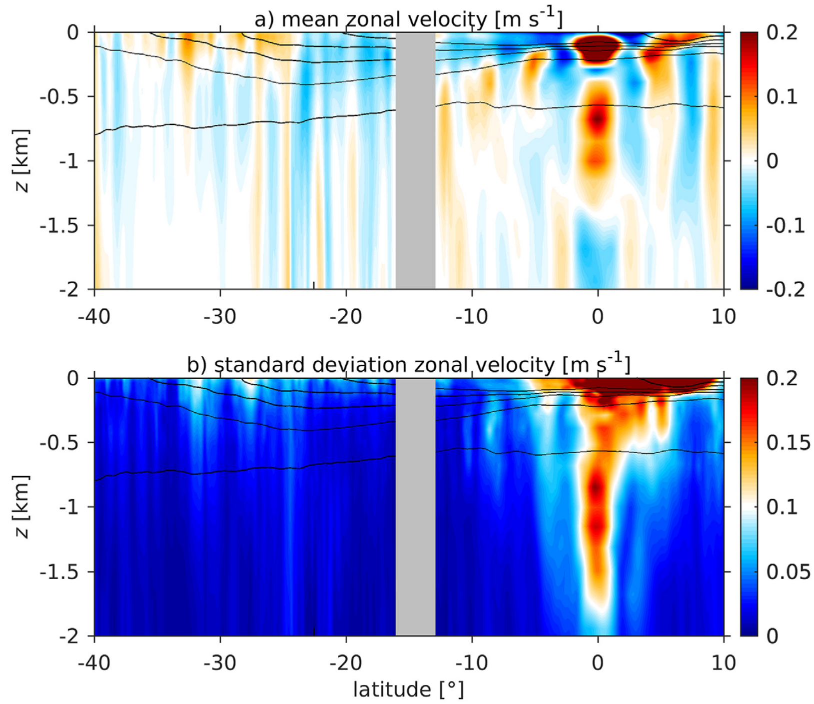

Figure 7. (a) Annual mean and (b) standard deviation of the zonal velocities along the western transects. Potential density, σ_2, is contoured every 1 kg m^{-3} (black curves). The gray bar marks the absence of data at the FPI.

stronger at higher latitudes. In the following, we will demonstrate that these monthly and annual cycles in *KE* and *N* mostly affect the internal tide propagation to the north of the FPI.

4.2. Taylor-Goldstein Approach

An internal tide signal measured at a fixed location can become incoherent due to temporal changes in its phase and amplitude. The loss of phase coherence of propagating internal tides can be attributed to refraction due to the time-varying background stratification, Doppler shifting by the time-varying subtidal current, and refraction due to time-varying background relative vorticity [*Zaron and Egbert*, 2014]. The

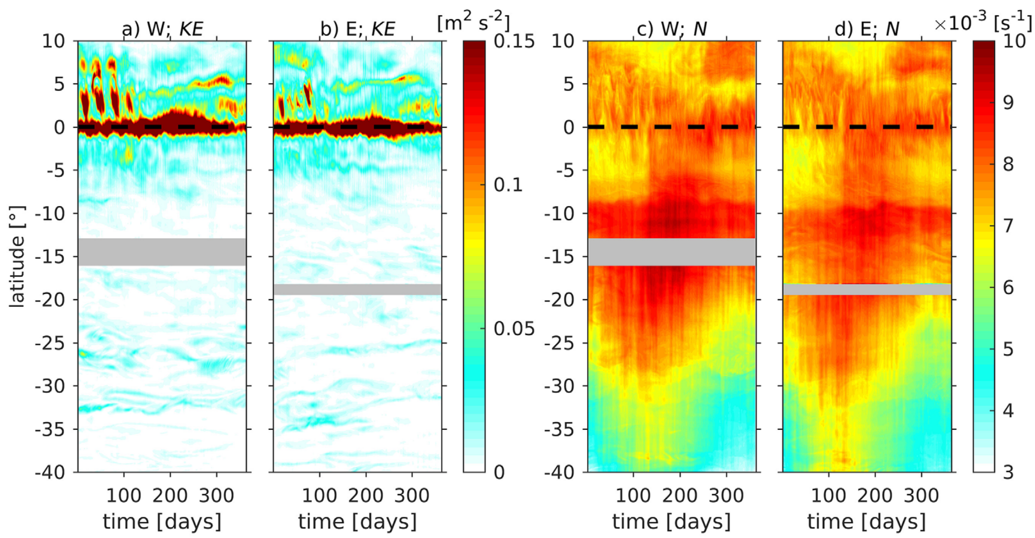

Figure 8. The annual evolution of the 2 day mean kinetic energy (a) and (b) and buoyancy frequency (c) and (d) averaged over the surface 500 m. The western (W) transects are shown in Figures 8a and 8c and the eastern (E) transects are shown in Figures 8b and 8d. The absence of data at the FPI is marked by the gray bars.

amplitude measured at a fixed location may vary in time as the mesoscale flow refracts and advects the internal wave beams over the measurement location [*Rainville and Pinkel*, 2006; *Dunphy and Lamb*, 2014; *Kelly and Lermusiaux*, 2016]. The amplitude can also change as the internal tide is affected by time varying dissipation along its path and by time-variable reflection.

In order to explain the internal tide incoherence near the FPI, we correlate the time variability of the internal-tide travel time along a beam with the incoherent fraction of the total flux. The travel time is obtained by integrating the phase speed along a beam. In this method, we can explain the incoherence due to phase speed variability, but not necessarily due to amplitude variability. We argue that the contribution of dissipation to the amplitude variability is small because the dissipation at the equator is not elevated in HYCOM (Figures 5 and 6). Similarly, most of the energy flux from the FPI is not reflected but transmitted across the equatorial jets (Figure 2 and supporting information). Only in the months of March and April does some energy from the northeast beam appear to be reflected southeastward near 230° E and 0° N (supporting information), although the energy flux could also represent transmitted internal tides from Hawaii. Most of the uncertainty in our approach may be associated with the meandering of the beams, which is captured by the incoherent flux fraction, but not necessarily by the travel-time variability, although the underlying phase speed variability may lead to beam meandering. In a large part of the study area, south of the equator, the lateral movement of the monthly-mean internal tide beams from the FPI is minimal, whereas the beams can move laterally by a few degrees to the north of the equator (see supporting information).

We compute long-wave phase speeds using the Taylor-Goldstein (TG) equation [*Miles*, 1961]

$$\frac{\partial^2 W}{\partial z^2}+\left(\frac{N^2}{(\bar{u}-c)^2}-\frac{1}{(\bar{u}-c)}\frac{\partial^2 \bar{u}}{\partial z^2}-k^2\right)W=0, \tag{8}$$

where W is the vertical velocity eigenfunction, c is the phase speed, N and $\bar{u}$ are the depth-dependent buoyancy frequency and background flow, and k is the horizontal wave number. N and $\bar{u}$ are assumed to vary only in the vertical, and c, $\bar{u}$, and k are directed along $\hat{x}$, i.e., in the direction of wave propagation. In this equation, the effect of rotation is ignored. The phase speeds are computed with a Matlab function that is freely available on the internet (http://salty.oce.orst.edu/wave_analysis/SSF_index.html) [*Smyth et al*., 2011]. The TG approach has been used successfully to estimate mode-one and mode-two phase speeds in sheared flow [*da Silva et al*., 2015; *Magalhaes et al*., 2016] and in geometric ray tracing of internal tides through a mesoscale eddy field [*Park and Farmer*, 2013].

The TG equation accounts for the depth-dependent stratification and vertically sheared horizontal background flow in the direction of propagation, while ignoring the contribution of the orthogonal velocities. Moreover, the two-dimensional TG equation does not include the effect of the background relative vorticity ξ. As in *Zaron and Egbert* [2014], we find that the effect of ξ, computed over 2 days and the surface 500 m, has a negligible effect on the semidiurnal internal tide propagation. M_2 internal tides are not trapped or reflected due to the effective Coriolis frequency [*Kunze*, 1985], $f_e=f+\xi/2$, where f is the local Coriolis frequency, because f_e/ω_2 ranges from -0.7 at 40°S to $+0.1$ at 10°N, where ω_2 is the M_2 frequency. The maximum absolute value of ξ/ω_2 is about 0.08 near 40°S, while it is about 0.04 in the equatorial jets.

The internal tides that radiate away from the FPI are predominantly mode-one waves. Hence, we compute mode-one phase speeds for 2 day mean fields of stratification and depth-dependent velocities along four transects for 1 year. The phase speeds are computed for three cases: (1) time-varying stratification and shear flow ($N+U$), (2) time-varying stratification only (N), and (3) time-varying shear flow with annual-mean stratification (U). The subtidal sheared and barotropic velocities are rotated along the transect. We note that the subtidal barotropic velocities have little influence on the TG-inferred phase speeds.

The transects coincide with the central axis of the bins in Figure 4a. We assume that the internal tides propagate along a linear transect. This assumption is not grossly violated as the horizontal wave rays are fairly linear in our area of interest. In our analysis, we do not trace the rays geometrically because this is too computationally expensive to do over an entire year and over such a large area. The horizontal scales of the internal waves are not much smaller than the scales of the mesoscale scale flows of $\mathcal{O}$(100 km). Hence, the geometric ray tracing approximation may not be valid as these scales cannot well be separated [*Zaron and Egbert*, 2014].

Table 1. Annual and Area-Mean Phase Speed c, Its Normalized Standard Deviation $\delta c/c$, Travel Time τ, and Its Normalized Standard Deviation $\delta\tau/T_{M2}$, Where T_{M2} Is the Tidal Period, for Four Nearfield and Far-Field Areas Along the Northwest (NW) and Southeast (SE) Transects[a]

		c (m s^{-1})			TGC		
Area	Latitude (°)	SL	TG	SSH	$\delta c/c$ (%)	τ (day)	$\delta\tau/T_{M2}$ (%)
Far-field NW	0.8	2.9	2.9	2.7	2.9	6.3	12.9
Near-field NW	−7.5	3.1	3.0	2.8	1.8	2.1	5.6
Near-field SE	−27.7	3.6	3.1	3.4	1.2	2.3	3.0
Far-field SE	−37.0	3.8	3.0	3.7	1.1	5.8	4.6

[a]The phase speeds are computed using the Stürm Liouville (SL) equation with Coriolis dispersion, the Taylor Goldstein equation without Coriolis dispersion (TG) and with a correction to account for Coriolis dispersion (TGC), and the plane-wave-fit method (SSH). The TG phase speed is for the case with time variable shear flow and stratification.

Coriolis dispersion increases the phase speed of internal waves at higher latitudes. As the TG phase speeds do not include Coriolis dispersion, the travel times will be longer than for the case with Coriolis dispersion. We compute the M_2 phase speeds for time and spatially varying and depth-dependent stratification using the Stürm-Liouville (SL) equation [*Gill*, 1982], which includes rotation, but no background flow. The difference between the annual and area-mean SL and uncorrected TG phase speeds is the largest along the southern transects (Table 1). To account for Coriolis dispersion, the TG phase speeds are corrected by removing the annual-mean TG speed and by adding the annual-mean SL speed at each coordinate.

Every M_2 tidal cycle, we track the progression of internal tide fronts radiating from the FPI along the four transects over 1 year. The phase speeds of these internal tides are interpolated from the spatially and temporally varying corrected TG phase speeds for the three cases. For each month and year, we compute travel-time standard deviations $\delta\tau$ along the transects and average them over the nearfield and far-field areas shown in Figure 4a. The travel times and standard deviations of the corrected TG speeds are smaller than the TG speeds without Coriolis dispersion, e.g., by about 20% along the southeast transect. However, the omission of this correction does not affect the results and conclusions. The annual-mean travel times to the midpoints of the nearfield and far-field areas are about 2 and 6 days (Table 1). As the travel time increases along the beam, its standard deviation, normalized by the M_2 tidal period T_{M2}, also increases due to the accumulated effects of the mesoscale variability (Table 1). The strong local mesoscale variability in the farfield of the northern transect is reflected in a relatively large normalized standard deviation of the TG phase speed $\delta c/c$, which contributes to the much larger $\delta\tau/T_{M2}$ of about 13%.

Time series of the area-averaged normalized travel time standard deviation $\delta\tau/T_{M2}$ are plotted alongside with the area-averaged ratio of the difference of the total and the coherent flux to the total flux (γ, equation (7)) for nearfield and far-field areas along the western and eastern transects in Figures 9 and 10. $\delta\tau/T_{M2}$ and γ are computed for each month and for 1 year. The annual values are marked by the gray bar and the "y" label in Figures 9 and 10. In the following sections, we consider the processes that drive the variability on monthly and annual time scales.

4.2.1. Monthly Time Scale

The agreement in space and time between the monthly travel-time standard deviation and the monthly mean flux incoherence fraction is fairly good along the four transects in Figures 9 and 10. For example, both $\delta\tau/T_{M2}$ and γ are larger in the farfield (dotted curves) than in the nearfield (curves with crosses) to the north of the FPI. To the south, there is no clear difference between the nearfield and far-field values of $\delta\tau/T_{M2}$ and γ. Both are much smaller than they are in the north, and $\delta\tau/T_{M2}$ due to shear flow and stratification ($N+U$; green curves) is equally attributed to currents (U; red curves) and stratification (N; blue curves).

The monthly mean flux incoherence portrays a seasonal variability in the farfield along the northwest transect with large incoherence in the months September to March and weaker and more variable incoherence from April to August (black dotted curve in Figure 9a). This pattern corresponds to large $\delta\tau/T_{M2}$ due to combined shear flow and stratification in the months September to February and weaker $\delta\tau/T_{M2}$ in the subsequent months ($N+U$; green dotted curve in Figure 9c). November is the month with the largest $\delta\tau$, which is about 18% of the M_2 tidal period. The correlation coefficient r between γ and $\delta\tau/T_{M2}$ in the farfield of the northwest transect is 0.81. In the first half of the year, $\delta\tau/T_{M2}$ due to $N+U$ can be mainly attributed to the shear flow (U), and less so to the stratification (N). The relative importance of the shear flow in $\delta\tau/T_{M2}$ clearly coincides with the large variability in surface kinetic energy associated with the tropical instability waves in

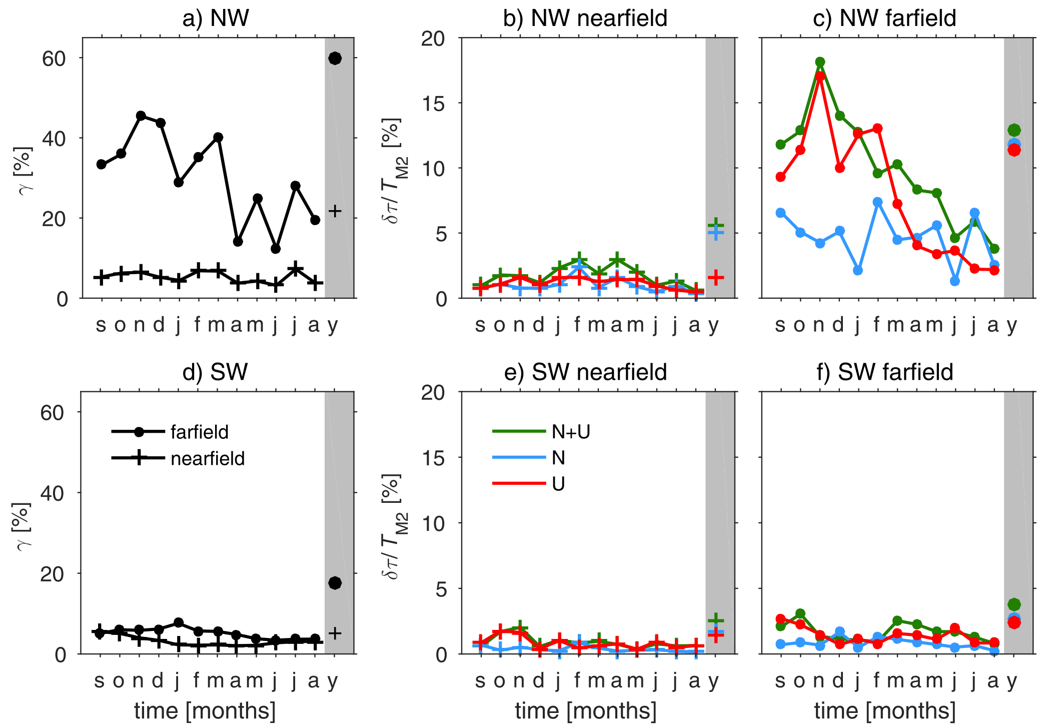

Figure 9. The ratio of the incoherent flux to the total flux (γ) in the nearfield and farfield (a) is compared to the normalized travel-time standard deviation $\delta\tau/T_{M2}$ in the nearfield (b) and far field (c) of the northwest (NW) transect. Subplots (d), (e), and (f) show the same but for the southwest transect. The travel-time standard deviation is normalized by the M_2 tidal period. $\delta\tau/T_{M2}$ is based on TG phase speeds due to sheared currents and stratification ($N+U$), stratification only (N), and sheared currents only (U). Values are averaged over the far-field areas (dots) and the nearfield areas (crosses), shown in Figure 4a, over the months September to August (s-a), and over an entire year (y). The annual value is highlighted by the gray background.

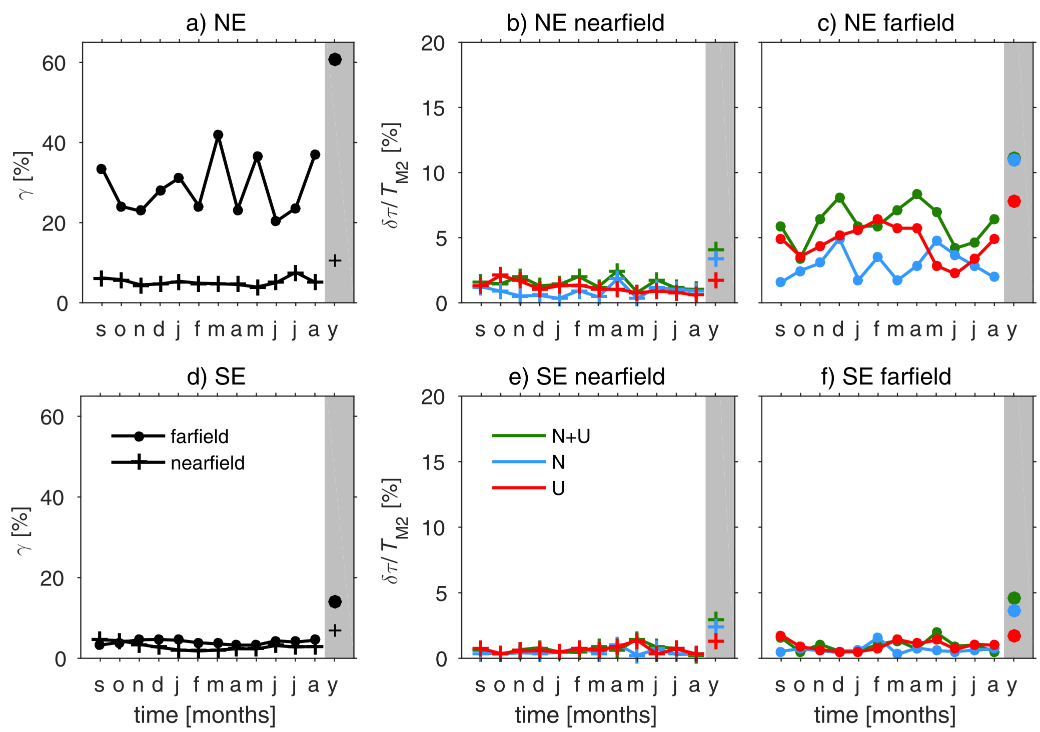

Figure 10. As in Figure 9, but for the northeast (NE) and southeast (SE) transects.

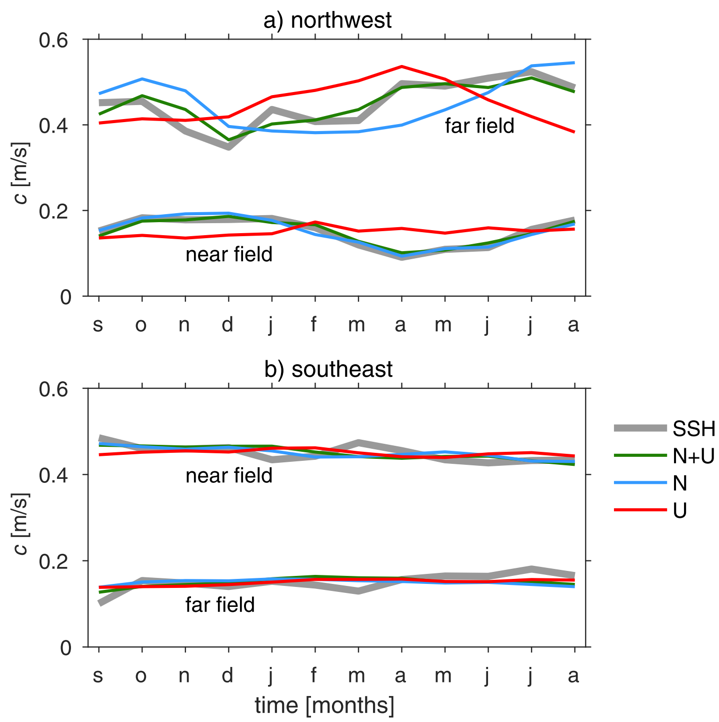

Figure 11. The monthly phase speeds from September to August (s-a) for the nearfield and far-field computed along the (a) northwest and (b) southeast transects. The phase speeds are computed by integrating phases extracted from plane wave fitting HYCOM sea surface heights (gray curves) and by using the TG approach for sheared currents and stratification (green), stratification only (blue), and sheared currents only (red). To better facilitate a visual comparison, the mean phase speeds are removed and the far-field and nearfield time series are offset by 0.15 or 0.45 m s^{-1}.

Figure 8a (0–120 days, 0$-$7°N), which have periods of 30–40 days. In the second half of the year, $\delta\tau/T_{M2}$ is more equally attributed to currents and stratification.

In the farfield of the northeast transect (Figure 10a), the monthly mean flux incoherence does not show a strong seasonal variability as compared to the northwest transect: γ is about 35$\pm$10%. In accordance, the monthly travel-time standard deviations for the three TG cases also lack a clear seasonal cycle in the farfield of the northeast transect (Figure 10c). As with the northwest transect, the shear flow still contributes more to $\delta\tau/T_{M2}$ than the stratification. The correlation coefficient between γ and $\delta\tau/T_{M2}$ due to $N+U$ in the farfield of the northeast transect is 0.38. The lack of seasonal variability in γ and $\delta\tau/T_{M2}$ can be attributed to the weaker seasonal variability in the kinetic energy due to the tropical instability waves along the northeast transect as compared to the northwest transect (Figures 8a and 8b).

4.2.2. Annual Time Scale

On an annual time scale, the flux incoherence fraction and the normalized travel-time standard deviation are generally larger than on monthly time scales: see "y" values in Figures 9 and 10. Both the annual values of γ and $\delta\tau/T_{M2}$ are generally larger in the farfield than in the nearfield and they are larger along the northern than along the southern transects. Compared to monthly time scales, the contribution of stratification to $\delta\tau/T_{M2}$ on an annual time scale has become more important than the annual contribution of the shear flow. This is in qualitative agreement with Figure 8 that shows that surface kinetic energy near the equator features monthly and annual cycles, while stratification mostly changes on an annual (i.e., seasonal) time scale.

In the following, we consider the processes determining the magnitude of the annual value of $\delta\tau/T_{M2}$, which is due to the underlying phase speed variability. We compute the monthly-mean phase speeds over 12 ensembles of 15 two-day mean TG phase speeds. The monthly mean TG speeds for time-varying stratification and shear flow, time-varying stratification only, and time-varying shear flow with an annual-mean stratification along the nearfield and far-field areas of the northwest and southeast transect are plotted in Figure 11 (the northeast and southwest transects feature similar phase speed variability and are not shown). For the best comparison, the annual-mean speeds are removed and the nearfield and far-field values are offset from zero by 0.15 or 0.45 m s^{-1} in Figure 11.

The largest seasonal variability occurs in the far-field and nearfield areas of the northwest transect (Figure 11a), while little (seasonal) phase-speed variability occurs along the southeast transect (Figure 11b), in accordance with small $\delta\tau/T_{M2}$ in Figures 10e and 10f. In the farfield of the northwest transect, the variability in the TG phase speeds for $N+U$ is due to the combined variability in the stratification (N) and shear flow (U) (Figure 11a). The equal contribution of stratification and shear flow is reflected in the annual values of

$\delta\tau/T_{M2}$ in Figure 9c. In contrast, in the nearfield of the northwest transect the variability in stratification is the dominant cause of the phase speed variability; the N curve mostly follows the $N+U$ curve in Figure 11a. This is also shown in Figure 9b, where $\delta\tau/T_{M2}$ due to stratification is larger than due to shear flow.

4.3. Plane-Wave Fit Method

How does the annual variability in the monthly-mean phase speeds compare with the actual internal tide propagation celerities in the HYCOM simulation? The internal tide phase speeds can be computed from the spatially varying steric sea surface height phases of the internal tides by phase integration along the wave beam:

$$c_{SSH} = \frac{\omega_2 \int ds}{\int d\phi}, \tag{9}$$

where ϕ is the unwrapped phase and s is the coordinate along the wave beam. However, when multiple wave modes from different directions are superposed, standing wave patterns appear in the phase maps [*Rainville et al*., 2010], complicating the phase speed calculation. In order to accurately compute the phase speed, one needs to integrate the phase of the same wave. Hence, we follow the plane-wave fitting approach of *Zhao and Alford* [2009] and *Zhao et al*. [2016], in which mode-one plane waves from different directions can be separated. In the plane-wave fit method, the local mode-one wave number k and wave propagation direction are prescribed, whereas the wave amplitude and phase are computed with a least-squares fit. As a first step, we extract M_2 amplitudes and phases for the steric sea surface height of HYCOM for each month over an entire year. For fitting windows with a size of about 1.5 times the local mode-one wave length, a plane wave is fitted to the sea surface height time series for 1° directional increments. The local mode-one wave length is computed by solving the SL equation. Mode-one wave lengths vary from about 130 km at the equator to about 190 km at 45°S. Phases of the waves with the three largest amplitudes are extracted within a range of $\pm 30°$ around the direction of each transect. We use this $\pm 30°$ range because we are only interested in capturing waves that propagate away from the FPI. The phase $\phi(x, y)$ of the wave with the largest amplitude is used for the phase speed calculation (equation (9)). The fitting windows are moved in increments of several grid sizes within the HYCOM domain. We can only reliably compute mode-one phase speeds along the northwest and southeast transects. The performance of the plane-wave method may be adversely impacted by mesoscale variability, by imperfections in the separation of waves from closely aligned directions, and/or by mismatches between the prescribed SL and HYCOM simulated wave numbers. This may cause phase jumps invalidating the phase speed calculation. Although not pursued here, we note that the phase speed $c_{SSH} = \omega_2/k$ along the beam can also be computed by estimating the wave number k from a two-dimensional wavenumber spectrum of steric sea surface height [*Ray and Zaron*, 2016]. *Ray and Zaron* [2016] computed wave numbers for areas of ~2000 × 2000 km^2, which dimensions are at least twice as large as our nearfield and far-field areas. It is unclear if wave numbers and phase speeds can be reliably estimated with the spectral method for these smaller areas.

The plane-wave-fit-derived phase speeds are shown as the gray curves in Figures 11a and 11b. The agreement between the TG phase speeds for $N+U$ and the sea surface height-based phase speeds is quite good along both transects, providing confidence in our simple TG model. The large TG phase speed variability along the northwest transect and the lack thereof along the southeast transect is well-captured by the plane-wave fit method. The correlation coefficients between c_{N+U} and c_{SSH} in the nearfield and farfield of the northwest transect are $r = 0.97$ and $r = 0.90$, respectively.

The annual-mean phase speeds of the plane-wave fit method increase poleward from about 2.7 m s^{-1} in the farfield of the northwest transect to 3.7 m s^{-1} in the farfield of the southeast transect, mainly due to Coriolis dispersion (Table 1). These rates compare fairly well with the SL phase speeds, but the SL speeds are up to 10% larger than the plane-wave fitted celerities.

5. Discussion and Conclusions

In this paper we have computed total, coherent, and incoherent energy fluxes associated with semidiurnal internal tides propagating across the equatorial Pacific Ocean in a global ocean simulation forced by atmospheric fields and astronomical tides. In agreement with altimetry observations of semidiurnal internal tide sea surface height amplitudes (Figure 1), we find that the coherent internal tides radiating equatorward from the French Polynesian Islands (FPI) and Hawaii are quite weak at the equator, i.e., their energy flux approaches zero (Figure 4b). In contrast, the coherent fluxes that radiate poleward from the FPI are not much smaller than the total fluxes.

At the FPI, the barotropic to baroclinic conversion is largely coherent with the barotropic tidal forcing on monthly and annual time scales (Figures 5d and 6d). This implies that the internal tides become incoherent as they propagate away from the FPI. This contrasts with the internal-tide generation in Luzon Strait, where up to 30% of the local generation is incoherent in a year-long model simulation [*Kerry et al*., 2016]. The internal tide generation in Luzon Strait is modulated by remotely generated internal tides from the Mariana Island Arc and by the time variability of the Kuroshio. Neither mesoscale currents nor remote internal tides strongly impact the local internal tide generation at the FPI. However, the time variability of the jets and the tropical instability waves at the equator has a large impact on the coherence of the internal tides propagating equatorward from the FPI.

The Pacific equatorial region is characterized by zonal jets with strong vertical and horizontal shear. The jets are modulated by tropical instability waves with periods of about 30–40 days (Figures 3 and 8) [*Philander et al*., 1986]. While the annual-mean coherent energy fluxes approach zero at the equator, the semidiurnal band-passed fluxes are not zero (Figures 5a and 6a). Hence, if our model results are correct, then the apparent demise of the internal tide at the equator seen in satellite altimetry maps is not solely associated with dissipation due to internal wave breaking. Our $1/12.5^\circ$ simulations suggest that the jets decohere the internal tides, but do not cause an increase in their dissipation (Figures 5c and 6c). However, the relatively coarse resolution of HYCOM may not optimally resolve the internal-tide dissipation processes that occur at the equator. Higher-resolution simulations may be needed to study the relevance of these dissipative processes.

The dissipation rates of the band-passed internal tide to the south of the FPI are higher than to the north. The enhanced dissipation in the south may be associated with a rougher seafloor [*Buijsman et al*., 2016], a disappearing wave guide due to a poleward reduction in stratification (see the poleward shoaling isopycnals in Figure 7), and a poleward declining group speed.

In the equatorial region near 220°E, along the northwest transect, we find that the fluxes are strongly incoherent in the period September 2011 to February 2012, while they are more coherent during the period from April to August 2012 (Figure 9a). This seasonal cycle in incoherence at this location corresponds with the seasonal cycle of westward propagating tropical instability waves (Figure 8a). Interestingly, about 10° to the east, along the northeast transect, the equatorward fluxes do not portray this seasonal variability in incoherence, coinciding with a reduced strength and activity of the tropical instability waves (Figure 8b).

We apply the Taylor-Goldstein equation to study the causes of the internal tide incoherence. We compute the variability of mode-one phase speeds along a beam due to the time-varying stratification and shear flow, time-varying stratification only, and time-varying shear flow with an annual-mean stratification. We integrate these phase speeds along the beam and compute standard deviations in the internal-tide travel time for each month and year. We find two distinct time scales that govern the internal tide incoherence. On time scales of about a month (the period of the tropical instability waves), the internal tide incoherence north of the FPI is mainly attributed to the time variability in the sheared flow associated with the jets. The amplitude of the tropical instability waves is larger in the period from September to February than in the period from April to August. As a consequence, the monthly standard deviation in the travel time due to the shear flow is also stronger in the former and weaker in the latter period (Figure 9c). The second time scale is associated with the annual variability in the travel time. North of the FPI, the annual travel-time standard deviation is due to a combination of seasonal variability in stratification and shear flow (farfield) and seasonal variability in stratification (nearfield) (Figure 11). In contrast, south of the FPI the incoherence is weak and no distinct monthly or seasonal cycles are present.

The Taylor-Goldstein approach can explain a significant part of the variability in the monthly-mean flux incoherence fraction along the northern transects (up to $r^2=66\%$; Figures 9 and 10). The remainder may be attributed to the fact that the two-dimensional Taylor-Goldstein approach ignores three-dimensional effects and that incoherence due to internal tide amplitude variability in a fixed point, e.g., due to beam meandering, has not been explicitly accounted for.

We apply a plane-wave-fit method to steric sea-surface height amplitude and phase to compute monthly mean phase speeds of unidirectional plane waves. The seasonal time variability of these phase speeds compares well with the phase speeds computed with the Taylor-Goldstein approach for time-varying stratification and shear flow along northern and southern transects (Figure 11).

Seasonal changes in internal tide parameters, such as sea surface height amplitude, have been mostly attributed to seasonal changes in stratification. In a realistically forced global model study, *Müller et al*. [2012] find seasonal variability in internal tide amplitudes in all ocean basins, including the region around the FPI. *Shriver et al*. [2014] performed harmonic fits to sea surface height internal tide amplitudes from earlier global HYCOM simulations performed prior to the simulation used in this study and found strong seasonal variability in the amplitude between the equator and the FPI. This location coincides with our nearfield bin along the northwest transect, where we also find a seasonal cycle with an annual period in phase speed due to changes in stratification (Figure 11a). In a tidal modeling study of the Hawaiian archipelago, *Zaron and Egbert* [2014] find that 10% of the phase speed variance over 8 years can be attributed to seasonal cycles in stratification, whereas the remainder is due to variability in mesoscale stratification. In this paper we demonstrate that in addition to stratification, temporal variability in shear flow is also an important contributor to internal tide incoherence on both monthly and annual time scales.

In the study by *Zaron and Egbert* [2014], internal-tide phase speed variability due to stratification dominates over the contribution due to Doppler shifting of surface mean flows near Hawaii. *Zaron and Egbert* [2014] argue that the smooth mesoscale fields used for the initialization of their simulations are the cause of the weaker contribution of the Doppler shifting. In our realistically forced HYCOM simulations with a horizontal resolution of 8 km sharper mesoscale fronts occur than in the simulations by *Zaron and Egbert* [2014]. This may be one reason why the variability in vertically sheared flow fields is relevant for the phase speed variance in our study. Another reason may be that our simple Taylor-Goldstein model is slightly more advanced than *Zaron and Egbert* [2014]'s approach, as our approach considers the effect of vertically sheared horizontal flow. On monthly time scales, we find that most of the internal tide incoherence near the equator is due to the effect of the shear flow, while on longer (annual) time scales the influence of stratification becomes equally or more important.

Our results are in agreement with model studies by *Dunphy and Lamb* [2014], *Ponte and Klein* [2015], *Kerry et al*. [2016], *Kelly and Lermusiaux* [2016], and *Kelly et al*. [2016], who show that mesoscale structures such as eddies and jets can decohere, reflect, refract, and scatter the internal tides. We observe all of these mechanisms in the equatorial jet region, but we do not detect clear examples of wave reflections. The incident angle of the internal tides from the FPI is about 70° counterclockwise relative to the eastward flowing Equatorial Undercurrent. *Kelly and Lermusiaux* [2016] show that a barotropic Gulf Stream does not reflect internal tides if the angle of incidence is approximately $>70^\circ$ and $<125^\circ$. Although the incident internal tides at the equator barely satisfy this relation, the equatorial jets are not very barotropic, potentially affecting the reflection of internal tides.

Finally, we remark that in our HYCOM simulations, the effects described here are also seen in other equatorial regions. Outside the Pacific, the equatorial currents in the Atlantic and Indian Oceans also cause a strong decoherence of the internal tides radiating from, e.g., the Amazon shelf and the Andaman and Nicobar Islands, respectively. Consistent with the results described here, the prominence of the equator in maps of incoherent internal tides can also be seen in maps made from satellite altimetric [*Zaron*, 2017] and modeled [*Savage et al*., 2017] sea surface heights.

Acknowledgments
The three-dimensional output files for the model simulation analyzed in this paper are archived at the Department of the Navy Shared Resources Center (DSRC) at the Stennis Space Center. The files stored there can be accessed after obtaining an account at the facility. M.C. Buijsman, the corresponding author, can be contacted for information to access the archived data once an account has been established. M.C. Buijsman can provide access to two-dimensional postprocessed data sets that are stored on servers at the University of Southern Mississippi. We gratefully thank E. Zaron and two anonymous reviewers for comments on earlier versions of this paper. M. C. Buijsman acknowledges support from the Office of Naval Research under awards N00014–09-1–0832 and N00014–15-1–2288. J. G. Richman, J. F. Shriver, A. J. Wallcraft, and L. Zamudio thank ONR for supporting this work under program element 0602435N. B. K. Arbic thanks ONR for support under grant numbers N00014–11-1–0487 and N00014–15-1–2288. This work was supported in part by a grant of computer time from the DOD High Performance Computing Modernization Program at the Navy DSRC. The Naval Research Laboratory contribution number is NRL/JA/7320-17-3446.

References

Alford, M. H. (2003), Redistribution of energy available for ocean mixing by long-range propagation of internal waves, *Nature*, *423*, 159–162.

Ansong, J. K., B. K. Arbic, M. C. Buijsman, J. G. Richman, J. F. Shriver, and A. J. Wallcraft (2015), Indirect evidence for substantial damping of low-mode internal tides in the open ocean, *J. Geophys. Res. Oceans*, *120*, 6057–6071, doi:10.1002/2015JC010998.

Ansong, J. K., et al. (2017), Semidiurnal internal tide energy fluxes and their variability in a Global Ocean Model and moored observations, *J. Geophys. Res. Oceans*, *122*, 1882–1900, doi:10.1002/2016JC012184.

Arbic, B. K., S. T. Garner, R. W. Hallberg, and H. L. Simmons (2004), The accuracy of surface elevations in forward global barotropic and baroclinic tide models, *Deep Sea Res., Part II*, *51*, 3069–3101.

Arbic, B. K., A. Wallcraft, and E. Metzger (2010), Concurrent simulation of the eddying general circulation and tides in a global ocean model, *Ocean Modell.*, *32*, 175–187.

Arbic, B. K., J. Richman, J. Shriver, P. Timko, E. J. Metzger, and A. J. Wallcraft (2012), Global modeling of internal tides within an eddying ocean general circulation model, *Oceanography*, *25*, 20–29.
Becker, J. J., et al. (2009), Global bathymetry and elevation data at 30 arc seconds resolution: Srtm30_plus, *Mar. Geod.*, *32*, 355–371, doi:10.1080/01490410903297766.
Buijsman, M. C., J. M. Klymak, S. Legg, M. H. Alford, D. Farmer, J. A. MacKinnon, J. D. Nash, J.-H. Park, A. Pickering, and H. Simmons (2014), Three dimensional double ridge internal tide resonance in Luzon Strait, *J. Phys. Oceanogr.*, *44*, 850–869.
Buijsman, M. C., B. K. Arbic, J. A. M. Green, R. W. Helber, J. G. Richman, J. F. Shriver, P. G. Timko, and A. J. Wallcraft (2015), Optimizing internal wave drag in a forward barotropic model with semidiurnal tides, *Ocean Modell.*, *85*, 42–55.
Buijsman, M. C., J. K. Ansong, B. K. Arbic, J. G. Richman, J. F. Shriver, P. G. Timko, A. J. Wallcraft, C. Whalen, and Z. Zhao (2016), Impact of internal wave drag on the semidiurnal energy balance in a global ocean circulation model, *J. Phys. Oceanogr.*, *46*, 1399–1419.
Carrére, L., C. Le Provost, and F. Lyard (2004), On the statistical stability of the M_2 barotropic and baroclinic tidal characteristics from along-track TOPEX/Poseidon satellite altimetry analysis, *J. Geophys. Res.*, *109*, C03033, doi:10.1029/2003JC001873.
Chavanne, C., P. Flament, D. Luther, and K.-W. Gurgel (2014), The surface expression of semidiurnal internal tides near a strong source at Hawaii. Part II: Interactions with mesoscale currents, *J. Phys. Oceanogr.*, *40*, 1180–1200.
Colosi, J. A., and W. Munk (2006), Tales of the venerable Honolulu tide gauge, *J. Phys. Oceanogr.*, *36*, 967–996.
da Silva, J., M. Buijsman, and J. Magalhaes (2015), Internal waves on the upstream side of a large sill of the Mascarene Ridge: A comprehensive view of their generation mechanisms and evolution, *Deep Sea Res., Part I*, *99*, 87–104.
Dunphy, M., and K. G. Lamb (2014), Focusing and vertical mode scattering of the first mode internal tide by mesoscale eddy interaction, *J. Geophys. Res. Oceans*, *119*, 523–536, doi:10.1002/2013JC009293.
Dushaw, B. D., B. M. Howe, B. D. Cornuelle, P. F. Worcester, and D. S. Luther (1995), Barotropic and baroclinic tides in the central north Pacific Ocean determined from long-range reciprocal acoustic transmissions, *J. Phys. Oceanogr.*, *25*, 631–647.
Egbert, G. D., A. Bennett, and M. Foreman (1994), Topex/poseidon tides estimated using a global inverse model, *J. Geophys. Res.*, *99*, 821–852.
Firing, E., S. E. Wijffels, and P. Hacker (1998), Equatorial subthermocline currents across the Pacific, *J. Geophys. Res.*, *103*, 21,413–21,423.
Fu, L.-L., and C. Ubelmann (2014), On the transition from profile altimeter to swath altimeter for observing global ocean surface topography, *J. Atmos. Oceanic Technol.*, *31*, 560–568.
Garner, S. T. (2005), A topographic drag closure built on an analytical base flux, *J. Atmos. Sci.*, *62*, 2302–2315.
Gill, A. (1982), *Atmosphere-Ocean Dynamics, International Geophysics*, Academic Press, San Diego, Calif.
Hendershott, M. C. (1972), The effects of solid earth deformation on global ocean tides, *Geophys. J. R. Astron. Soc.*, *29*, 389–402.
Hogan, T. F., et al. (2014), The Navy Global Environmental Model, *Oceanography*, *27*, 116–125.
Holmes, R. M., J. N. Moum, and L. N. Thomas (2016), Evidence for seafloor-intensified mixing by surface-generated equatorial waves, *Geophys. Res. Lett.*, *43*, 1202–1210, doi:10.1002/2015GL066472.
Ivanov, V., L. Ivanov, and A. Lisichenok (1990), Redistribution of energy of the internal tidal wave in the North Equatorial Countercurrent region, *Sov. J. Phys. Oceanogr.*, *1*, 383–386.
Jayne, S. R. (2009), The impact of abyssal mixing parameterizations in an ocean general circulation model, *J. Phys. Oceanogr.*, *39*, 1756–1775.
Jayne, S. R., and L. C. St. Laurent (2001), Parameterizing tidal dissipation over rough topography, *Geophys. Res. Lett.*, *28*, 811–814.
Kantha, L. H., and C. C. Tierney (1997), Global baroclinic tides, *Prog. Oceanogr.*, *40*, 163–178.
Kelly, S. M., and P. F. J. Lermusiaux (2016), Internal-tide interactions with the Gulf Stream and Middle Atlantic Bight shelfbreak front, *J. Geophys. Res. Oceans*, *121*, 6271–6294, doi:10.1002/2016JC011639.
Kelly, S. M., N. L. Jones, G. N. Ivey, and R. J. Lowe (2015), Internal-tide spectroscopy and prediction in the Timor Sea, *J. Phys. Oceanogr.*, *45*, 64–83.
Kelly, S. M., P. F. J. Lermusiaux, T. F. Duda, and P. J. Haley Jr. (2016), A Coupled-mode Shallow Water model for tidal analysis: Internal-tide reflection and refraction by the Gulf Stream, *J. Phys. Oceanogr.*, *46*, 3661–3679, doi:10.1175/JPO-D-16-0018.1.
Kerry, C., B. Powell, and G. Carter (2014), The impact of subtidal circulation on internal-tide generation and propagation in the Philippine Sea, *J. Phys. Oceanogr.*, *44*, 1386–1405.
Kerry, C., B. Powell, and G. Carter (2016), Quantifying the incoherent M_2 internal tide in the Philippine Sea, *J. Phys. Oceanogr.*, *46*, 2483–2491.
Kunze, E. (1985), Near-inertial wave propagation in geostrophic shear, *J. Phys. Oceanogr.*, *15*, 544–565.
MacKinnon, J. A., M. H. Alford, O. Sun, R. Pinkel, Z. Zhao, and J. Klymak (2013), Parametric subharmonic instability of the internal tide at 29N, *J. Phys. Oceanogr.*, *43*, 17–28.
MacKinnon, J. A et al. (2017), Climate process team on internal-wave driven ocean mixing, *Bull. Am. Meteorol. Soc.*, doi:10.1175/BAMS-D-16-0030.1, in press.
Magalhaes, J. M., J. C. B. da Silva, M. C. Buijsman, and C. A. E. Garcia (2016), Effect of the North equatorial counter current on the generation and propagation of internal solitary waves off the Amazon shelf (SAR observations), *Ocean Sci. Discuss.*, *12*, 243–255.
Martini, K. I., M. H. Alford, J. Nash, E. Kunze, and M. A. Merrifield (2007), Diagnosing a partly standing internal wave in Mamala Bay, Oahu, *Geophys. Res. Lett.*, *34*, L17604, doi:10.1029/2007GL029749.
Mathur, M., G. S. Carter, and T. Peacock (2014), Topographic scattering of the low-mode internal tide in the deep ocean, *J. Geophys. Res. Oceans*, *119*, 2165–2182, doi:10.1002/2013JC009152.
Melet, A., R. Hallberg, S. Legg, and K. Polzin (2013), Sensitivity of the ocean state to the vertical distribution of internal-tide-driven mixing, *J. Phys. Oceanogr.*, *43*, 602–615.
Miles, J. (1961), On the stability of heterogeneous shear flows, *J. Fluid Mech.*, *10*, 496–508.
Moum, J. N., A. Perlin, J. D. Nash, and M. J. McPhaden (2013), Seasonal sea surface cooling in the equatorial Pacific cold tongue controlled by ocean mixing, *Nature*, *500*, 64–67.
Muench, J. E., and E. Kunze (2000), Internal wave interactions with equatorial deep jets. Part II: Acceleration of the jets, *J. Phys. Oceanogr.*, *30*, 2099–2110.
Müller, M., J. Cherniawsky, M. Foreman, and J.-S. von Storch (2012), Global map of M_2 internal tide and its seasonal variability from high resolution ocean circulation and tide modelling, *Geophys. Res. Lett.*, *39*, L19607, doi:10.1029/2012GL053320.
Müller, M., B. Arbic, J. Richman, J. Shriver, E. Kunze, R. B. Scott, A. Wallcraft, and L. Zamudio (2015), Toward an internal gravity wave spectrum in global ocean models, *Geophys. Res. Lett.*, *42*, 3474–3481, doi:10.1002/2015GL063365.
Müller, P., G. Holloway, F. Henyey, and N. Pomphrey (1986), Nonlinear interactions among internal gravity waves, *Rev. Geophys.*, *24*, 493–536.

Munk, W., and C. Wunsch (1998), Abyssal recipes II: Energetics of tidal and wind mixing, *Deep Sea Res., Part I*, *45*, 1977–2010.
Munk, W. H., and D. E. Cartwright (1966), Tidal spectroscopy and prediction, *Philos. Trans. R. Soc. London A*, *259*, 533–581.
Nash, J. D., E. Shroyer, S. Kelly, M. Inall, T. Duda, M. Levine, N. Jones, and R. Musgrave (2012a), Are any coastal internal tides predictable?, *Oceanography*, *25*, 80–95.
Nash, J. D., S. M. Kelly, E. L. Shroyer, J. N. Moum, and T. F. Duda (2012b), The unpredictable nature of internal tides on continental shelves, *J. Phys. Oceanogr.*, *42*, 1981–2000.
Ngodock, H. E., I. Souopgui, A. J. Wallcraft, J. G. Richman, J. F. Shriver, and B. K. Arbic (2016), On improving the accuracy of the barotropic tides embedded in a high-resolution global ocean circulation model, *Ocean Modell.*, *97*, 16–26.
Park, J.-H., and D. Farmer (2013), Effects of Kuroshio intrusions on nonlinear internal waves in the South China Sea during winter, *J. Geophys. Res. Oceans*, *118*, 7081–7094, doi:10.1002/2013JC008983.
Park, J.-H., and D. R. Watts (2006), Internal Tides in the Southwestern Japan/East Sea, *J. Phys. Oceanogr.*, *36*, 22–34.
Peters, H., M. C. Gregg, and J. M. Toole (1988), On the parameterization of equatorial turbulence, *J. Geophys. Res.*, *93*, 1199–1218.
Philander, S. G. H., W. J. Hurlin, and R. C. Pacanowski (1986), Properties of long equatorial waves in models of the seasonal cycle in the tropical Atlantic and Pacific Oceans, *J. Geophys. Res.*, *91*, 207–214.
Pickering, A., M. Alford, J. Nash, L. Rainville, M. Buijsman, D. Ko, and B. Lim (2015), Structure and variability of internal tides in Luzon Strait, *J. Phys. Oceanogr.*, *45*, 1574–1594.
Ponte, A. L., and P. Klein (2015), Incoherent signature of internal tides on sea level in idealized numerical simulations, *Geophys. Res. Lett.*, *42*, 1520–1526, doi:10.1002/2014GL062583.
Rainville, L., and R. Pinkel (2006), Propagation of low-mode internal waves through the ocean, *J. Phys. Oceanogr.*, *36*, 1220–1236.
Rainville, L., T. M. S. Johnston, G. S. Carter, M. A. Merrifield, R. Pinkel, P. F. Worcester, and B. D. Dushaw (2010), Interference pattern and propagation of the M_2 internal tide south of the Hawaiian Ridge, *J. Phys. Oceanogr.*, *40*, 311–325.
Ray, R. D. (1998), Ocean self-attraction and loading in numerical tidal models, *Mar. Geod.*, *21*, 181–192.
Ray, R. D., and G. T. Mitchum (1997), Surface manifestation of internal tides in the deep ocean: Observations from altimetry and island gauges, *Prog. Oceanogr.*, *40*, 135–162.
Ray, R. D., and E. D. Zaron (2011), Non-stationary internal tides observed with satellite altimetry, *Geophys. Res. Lett.*, *38*, L17609, doi:10.1029/2011GL048617.
Ray, R. D., and E. D. Zaron (2016), M_2 internal tides and their observed wavenumber spectra from satellite altimetry, *J. Phys. Oceanogr.*, *46*, 3–22.
Rosmond, T. E., J. Teixeira, M. Peng, T. F. Hogan, and R. Pauley (2002), Navy operational global atmospheric prediction system (NOGAPS): Forcing for ocean models, *Oceanography*, *15*, 99–108.
Savage, A. C., et al. (2017), Frequency content of sea surface height variability from internal gravity waves to mesoscale eddies, *J. Geophys. Res. Oceans*, *122*, 2519–2538, doi:10.1002/2016JC012331.
Shriver, J. F., B. K. Arbic, J. G. Richman, R. D. Ray, E. J. Metzger, A. J. Wallcraft, and P. G. Timko (2012), An evaluation of the barotropic and internal tides in a high resolution global ocean circulation model, *J. Geophys. Res.*, *117*, C10024, doi:10.1029/2012JC008170.
Shriver, J. F., J. G. Richman, and B. K. Arbic (2014), How stationary are the internal tides in a high-resolution global ocean circulation model?, *J. Geophys. Res. Oceans*, *119*, 2769–2787, doi:10.1002/2013JC009423.
Simmons, H. L., R. W. Hallberg, and B. K. Arbic (2004a), Internal wave generation in a global baroclinic tide model, *Deep Sea Res., Part II*, *51*, 3043–3068.
Simmons, H. L., S. R. Jayne, L. C. St. Laurent, and A. J. Weaver (2004b), Tidally driven mixing in a numerical model of the ocean general circulation, *Ocean Modell.*, *6*, 245–263.
Smyth, W. D., J. Moum, and J. Nash (2011), Narrowband, high-frequency oscillations at the equator: Part II: Properties of shear instabilities, *J. Phys. Oceanogr.*, *41*, 412–428.
Smyth, W. D., J. N. Moum, L. Li, and S. A. Thorpe (2013), Diurnal shear instability, the descent of the surface shear layer, and the deep cycle of equatorial turbulence, *J. Phys. Oceanogr.*, *43*, 2432–2455.
St. Laurent, L., and J. Nash (2004), An examination of the radiative and dissipative properties of deep ocean internal tides, *Deep Sea Res., Part II*, *51*, 3029–3042.
Stephenson, G. R., J. E. Hopkins, J. A. M. Green, M. E. Inall, and M. R. Palmer (2015), Baroclinic energy flux at the continental shelf edge modified by wind-mixing, *Geophys. Res. Lett.*, *42*, 1826–1833, doi:10.1002/2014GL062627.
van Haren, H. (2004), Incoherent internal tidal currents in the deep-ocean, *Ocean Dyn.*, *54*, 66–76.
Ward, M. L., and W. K. Dewar (2010), Scattering of gravity waves by potential vorticity in a shallow-water fluid, *J. Fluid Mech.*, *663*, 478–506.
Whalen, C. B., L. D. Talley, and J. A. MacKinnon (2012), Spatial and temporal variability of global ocean mixing inferred from Argo profiles, *Geophys. Res. Lett.*, *39*, L18612, doi:10.1029/2012GL053196.
Wunsch, C. (1975), Internal tides in the ocean, *Rev. Geophys.*, *13*, 167–182.
Zaron, E. D. (2015), Nonstationary internal tides observed using dual-satellite altimetry, *J. Phys. Oceanogr.*, *45*, 2239–2246, doi:10.1175/JPO-D-15-0020.1.
Zaron, E. D. (2017), Mapping the nonstationary internal tide with satellite altimetry, *J. Geophys. Res. Oceans*, *122*, 539–554, doi:10.1002/2016JC012487.
Zaron, E. D., and G. D. Egbert (2014), Time-variable refraction of the internal tide at the Hawaiian Ridge, *J. Phys. Oceanogr.*, *44*, 538–557.
Zhao, Z. (2016), Using CryoSat-2 altimeter data to evaluate M_2 internal tides observed from multisatellite altimetry, *Oceanography*, *121*, 5164–5180.
Zhao, Z., and M. H. Alford (2009), New altimetric estimates of mode-1 M_2 internal tides in the central North Pacific Ocean, *J. Phys. Oceanogr.*, *39*, 1669–1684.
Zhao, Z., M. Alford, J. Girton, L. Rainville, and H. Simmons (2016), Global observations of open-ocean mode-1 M_2 internal tides, *J. Phys. Oceanogr.*, *46*, 1657–1684.
Zilberman, N. V., M. A. Merrifield, G. S. Carter, D. S. Luther, M. D. Levine, and T. J. Boyd (2011), Incoherent nature of M_2 internal tide at the Hawaiian Ridge, *J. Phys. Oceanogr.*, *41*, 2021–2036.